Global and Planetary Change 244 (2025) 104623

Contents lists available at ScienceDirect

Global and Planetary Change

journal homepage: www.elsevier.com/locate/gloplacha

Clustered slumping in the northern South China Sea: Implications for chronology and geohazards

Yin Lu [a,*], Ed L. Pope [b], Qiliang Sun [c], Michael Strasser [d]

[a] State Key Laboratory of Marine Geology, Tongji University, 200092 Shanghai, China
[b] Department of Geography, Durham University, DH1 3LE Durham, UK
[c] College of Marine Science and Technology, China University of Geosciences (Wuhan), 430074 Wuhan, China
[d] Institute of Geology, University of Innsbruck, 6020 Innsbruck, Austria

ARTICLE INFO

Editor: Dr. Sun Jimin

Keywords:
Event deposits
Event-free age model
Sedimentary processes
South China Sea

ABSTRACT

Seismic facies analysis is the most widely used method to identify event deposits from subaqueous environments. However, the internal structures of a chaotic or transparent seismic unit that represent event deposits are usually poorly imaged. This is primarily due to the limited resolution (usually <10 m) of commonly available multi-channel seismic reflection data. As a consequence, potential (sub)meter-thick, interbedded background sediments that may divide the chaotic layer cannot be discerned on such a seismic profile. The result of this, is that a complex of multiple moderate-thickness event layers can be misinterpreted as a single, thick event layer and this can greatly impact age-depth model reconstruction and geohazard assessment. One approach to resolve the problem is to correlate seismic data with high-resolution sediment core analysis. To address the problem in the South China Sea, we combine multiple methods to identify event deposits in the IODP holes U1499A and U1432C. Our dataset reveals that: (1) the previously interpreted ~50 m-thick slumping unit in the region is a complex of multiple moderately sized units; (2) the slumping events are clustered between 0.6 and 0.4 Ma. Using our new understanding of event emplacement, we define event-free age models for mass wasting on the margin of the South China Sea, improving our understanding of local geohazards. Our methods here represent a sedimentological approach which could be used in other subaqueous environments to reconstruct event-free age models and geohazard histories.

1. Introduction

Seismic stratigraphic analysis is commonly employed to study lacustrine and marine depositional environments. Within the International Continental Scientific Drilling Program (ICDP) (Cukur et al., 2014; Coianiz et al., 2019) and the International Ocean Discovering Program (IODP) (Strasser et al., 2011), seismic reflection data is widely used to distinguish between large-scale mass movement deposits, such as slumping units and megaturbidites, from hemipelagic deposits. Parallel seismic reflections are usually interpreted to represent normal or background sediments which have not undergone postdeposition deformation and remobilization (Roksandić, 1978; Xu and Haq, 2022). In contrast, an interval characterized by chaotic and/or transparent seismic facies is usually interpreted as a mass movement deposit unit (Posamentier and Kolla, 2003; Frey Martinez et al., 2005; Bull et al., 2009). Together these data can be used to reconstruct the sedimentological history of a continental margin or lake basin.

Efforts have been made in recent decades to improve seismic reflection imaging. Generally, 2D multi-channel seismic reflection surveys can provide profiles with a vertical resolution of ~10 m, for example, the case from the South China Sea (He et al., 2014). This can be improved to the order of meters to decimeters by using 3D acoustic reflection techniques commonly now used in industry, (Strasser et al., 2011; Sun et al., 2017a) and advanced methods such as short-offset 3D "P-cable"-type geometry (Berndt et al., 2012; Karstens et al., 2019) and seismic diffraction imaging (Schwarz and Krawczyk, 2020; Ford et al., 2021), or high-resolution systems such as Sparker (Kluesner et al., 2018, 3.5 kHz (Olson and Damuth, 2010), etc.

However, despite the great improvement in acoustic reflection techniques, academic investigations, such as those associated with IODP drilling campaigns in the South China Sea, are still limited to lower resolution datasets. This continues to plague investigations concerning

* Corresponding author.
E-mail addresses: yinlu@tongji.edu.cn, yinlusedimentology@yeah.net (Y. Lu).

https://doi.org/10.1016/j.gloplacha.2024.104623
Received 12 June 2024; Received in revised form 31 October 2024; Accepted 2 November 2024
Available online 8 November 2024

chaotic seismic reflections and hence, thin interbedded background deposits often remain unresolvable on seismic profiles. As a result, where complexes of moderate-sized slumping units exist, these can be misrepresented as individual think slumping units. This will impact the accuracy of age-depth models for marine sections and therefore will affect potential geohazard assessments in subaqueous environments.

One possible approach to overcome these drawbacks in seismic interpretation is to correlate seismic stratigraphic data with high-resolution sedimentological analysis of long cores. Here, we apply this approach to drill cores from the northern South China Sea deep-basin (Fig. 1). In the basin, a ~ 50 m-thick chaotic seismic reflection within the seismic profile across the IODP Expedition 367 Site-U1499 has been interpreted as a thick slumping unit that occurred during ~0.8–0.4 Ma (Fig. 1c) (Sun et al., 2018c). Based on the assumption that this unit was a single instantaneous event deposit, the unit was entirely removed when establishing an astronomical-tuned age model using natural gamma-ray data (Zhang et al., 2019). In this paper, we test whether this ~50 m thick chaotic seismic reflection is indeed a consequence of a giant slump event or a complex of multiple smaller events. To achieve this, we analyze cores from IODP Expedition 367 Hole-U1499A and IODP Expedition 349 Hole-U1432C, which are 50 km apart from each other in the deep-basin (Fig. 1b). To do this we use detailed event sedimentological analysis. Based on our results, we then discuss wider implications of our results for event chronology reconstruction and geohazard assessment.

2. Geological setting

2.1. Northern edge of the South China Sea deep-basin

The South China Sea is one of the largest marginal seas in the world, with an area of ~3.5 million km^2, a maximum water depth of ~5500 m, and an average water depth of ~1200 m (Fig. 1a). It is located at the junction of the Pacific, Indo-Australian, and Eurasian Plates (Ding et al., 2018; Sun et al., 2019). It formed as a consequence of middle- to late-Cenozoic continental margin rifting (Larsen et al., 2018; Le Pourhiet et al., 2018; Ding et al., 2020). The South China Sea deep-basin receives >420 million tons of fluvial sediments every year from its northern margin, of which the Pearl River alone contributes >100 million tons annually (Milliman and Farnsworth, 2011; Liu et al., 2016).

The study area lies on the northern edge of the South China Sea deep-basin, a passive margin that comprises the Pearl River Canyon system, Baiyun Sag (continental slopes), and the nearby abyssal plain (Fig. 1b). The Pearl River Canyon system is slope-incising and slope-confined (Harris and Whiteway, 2011). The head of the system is incised into the continental slope, at a water depth of ~300 m, and ~ 250 km away from the mouth of the Pearl River. The head of this canyon did not

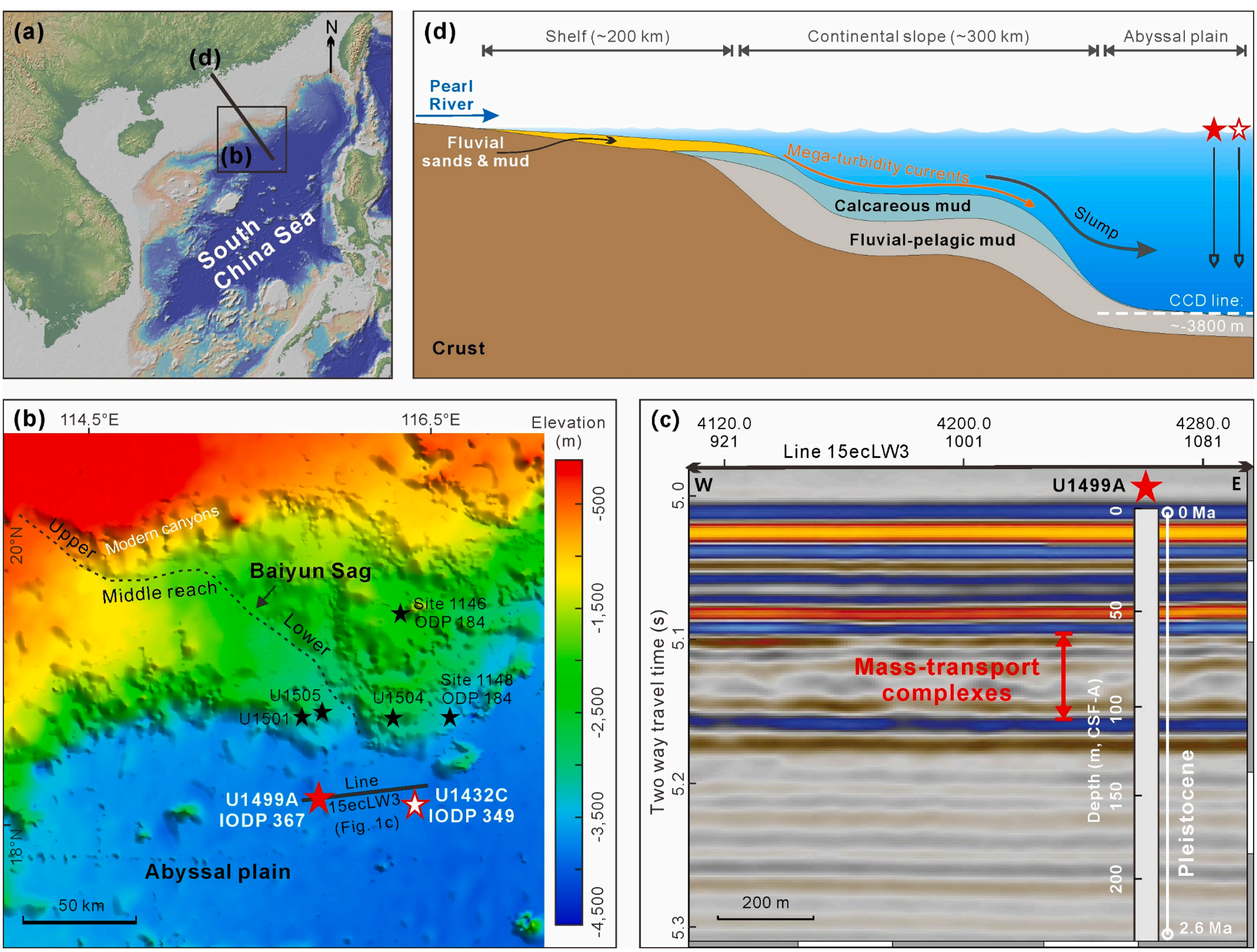

Fig. 1. Geological setting of the study area. (a) Locations of the South China Sea and focused study region. (b) Pearl River Canyon system (indicated by dashed black line), locations of IODP/ODP sites used (U1499 and U1432) and referred to (U1501, U1504, U1505, 1148 and 1146) in this study. (c) Seismic profile of crossline 15ecLW3 across Site U1499; the ~50 m-thick interval of mass-transport complexes is marked (adapted from Sun et al., 2018c); CSF-A: Core depth below sea floor-A. (d) A simplified model showing the sedimentary system and major sedimentary processes in the region. CCD: carbonate compensation depth.

connect to the Pearl River mouth during Quaternary eustatic sea level low stands when the sea level was ~130 m lower than today (Miller et al., 2020).

The Pearl River Canyon system extends over 250 km seaward down the continental slope and finally discharges onto the abyssal plain at a water depth of ~3500 m (Ding et al., 2013). Slope failures and turbidity currents have occurred frequently in this region (Fig. 1d). Many N-S extended sub-parallel short (~60 km) and deep (~50–300 m) canyons lie on the northern edge of the Baiyun Sag at water depths of ~450–1500 m (Zhu et al., 2010) (Fig. 1b). These canyons are relatively young and active when compared with the canyons developed in the middle and lower part of the Pearl River Canyon system. Small-scale landslides/slumps also repeatedly occurred in this region during the Quaternary (He et al., 2014).

The high fluvial sediment input, steep continental slopes, and deep canyons make the northern edge of the South China Sea deep-basin prone to slope failure and slumping (Ding et al., 2013; Wang et al., 2014; Wang et al., 2017; Li et al., 2020). In the middle-lower reach of the Pearl River Canyon system (Fig. 1b), Sun et al. (2008) first reported a large-scale submarine landslide complexes covering an area of ~13,000 km^2 by using multi-beam bathymetric mapping and seismic reflection data. By correlating with the strata at ODP site 1146 (Fig. 1b), the ages of those sliding events are estimated to be ~1.59 Ma, ~0.79 Ma, ~0.54 Ma, ~0.3 Ma, and ~ 0.19 Ma, respectively (Li et al., 2014; Sun et al., 2017b; Sun et al., 2018b).

2.2. IODP holes U1499A and U1432C

Two IODP holes on the northern edge of the abyssal plain near the Pearl River Canyon are used in this study (Fig. 1b). The 110 m Hole U1432C was cored at 3829 m water depth (18°21.08′N, 116°23.45′E), during the IODP Expedition 349 in 2014 (Li et al., 2015). The 659 m Hole U1499A was cored at 3760 m water depth (18°24.57′N, 115°51.59′E), during the IODP Expedition 367 in 2017 (Sun et al., 2018c). The two drill sites stand ~50 km apart on the abyssal plain, ideal for a detailed comparative study.

The site survey 2-D seismic reflection data shows a chaotic to transparent seismic layer tied to the core depth of ~100–50 m below the seafloor at Site U1499. The core interval has been interpreted as a thick slump unit deposited between ~0.8–0.4 Ma (Sun et al., 2018c) (Fig. 1c). This unit was then removed from astronomically-tuned age models generated for this site as is the common practice (Zhang et al., 2019).

Since the vertical resolution of the 2-D site seismic data used to survey the IODP sites is ~13 m (Sun et al., 2018b), sediment layers or features below this resolution (may represent ~100 kyr in time at the drill site) are unable to be clearly separated using this data. Thus, undisturbed pelagic mud intervals, turbidites, and volcanic ash layers with thickness below the seismic resolution cannot be discerned from the seismic data. Therefore, there is the possibility that the previously interpreted single thick slump unit comprises multiple layers of moderate- to large-scale slump deposits. If this is the case, a sedimentary sequence separated by undeformed pelagic mud, turbidite layers, and/or volcanic ash layers could be present (Fig. 2). This study will test this hypothesis by analyzing the sedimentary facies and structures from holes U1499A and U1432C, and conduct a detailed comparative study between the two sites.

3. Methods and primary chronology

For the purpose of this study, the upper 120 m of Hole U1499A and the entire 110 m of Hole U1432C are examined.

3.1. Depth-scale adjustment

Core recovery rates for some core sections are >100 %. This is due to the expansion of sediments during and after core extraction. To avoid missing centimeter-scale event layers, we adjust the originally documented depth scale (Depth CSF-A: core depth below sea floor-A; Li et al., 2015; Sun et al., 2018c) to corrected depth. This acknowledges any overlap of core sections post-expansion. A conversion table between the two depth scales is supplied in the supplementary information (Tables S1 and S2). All depths used in this study refer to the corrected depth scale if not annotated.

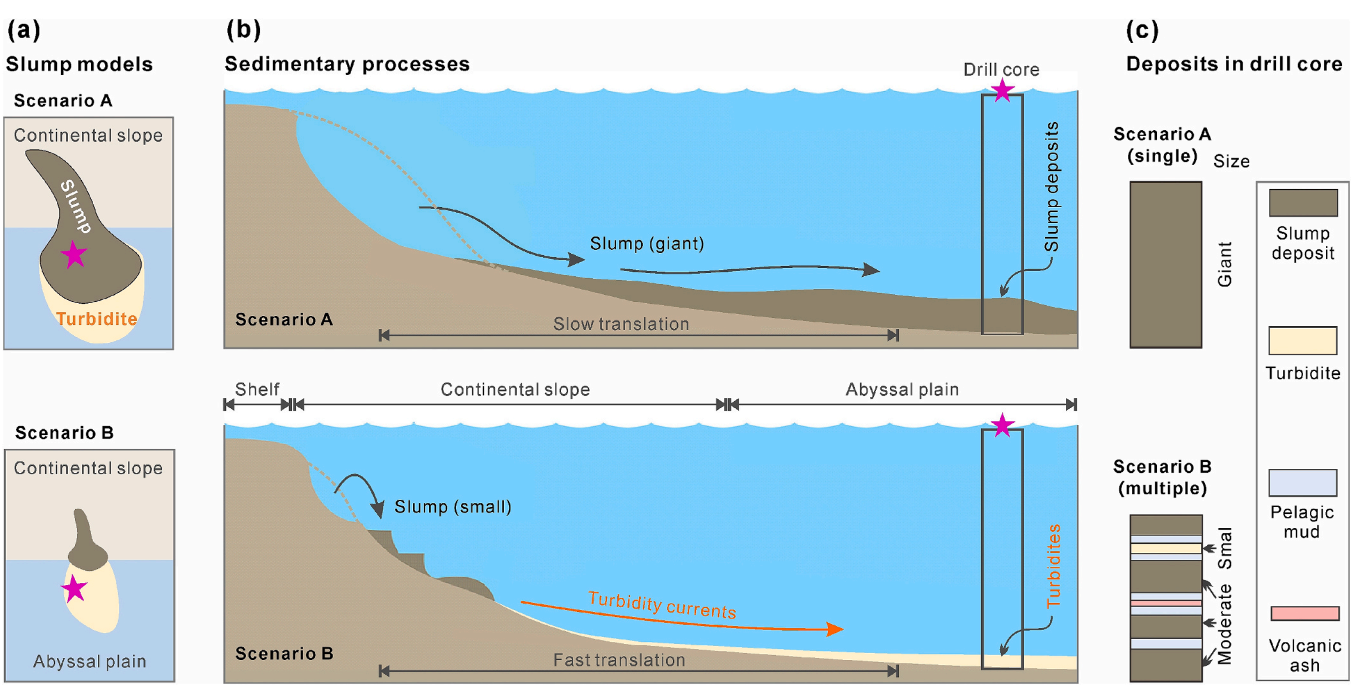

Fig. 2. Schematic figure explaining the hypothesis. (a) Two models of slumping: Scenario A, a giant slump; Scenario B, a series of small slumps. The stars indicate the locations of drill cores. (b) Sedimentary processes correspondence to the two slumping scenarios. (c) Event deposits correspondence to the two scenarios.

3.2. Magnetic susceptibility, bulk density, and natural gamma radiation measurements

The magnetic susceptibility of core sections was measured at 1 cm interval using a Bartington MS2F point sensor on a Section Half Multisensor Logger (Li et al., 2015; Sun et al., 2018c). Magnetic susceptibility is a useful proxy used to trace volcanic ash layers (Heider et al., 1993; Vigliotti et al., 2022). The bulk density of recovered sediments was evaluated based on measurements of gamma-ray attenuation. Gamma-ray attenuation was measured on whole-round core sections using a Multisensor Core Logger (Li et al., 2015; Sun et al., 2018c). It was measured at 2 cm and 2.5 cm resolution for holes U1499A and U1432C, respectively. Natural gamma radiation (counts per second) of sediments from holes U1499A and U1432C was measured on whole-round cores at 10 cm resolution using a Natural Gamma Radiation Logger (Li et al., 2015; Sun et al., 2018c). Natural gamma radiation is effective for stratigraphic correlation and helpful for the evaluation of the relative content of clay and carbonate (Díaz-Curiel et al., 2021; Liu et al., 2023).

3.3. Identification of event deposits and sediment facies

We identified sediment facies and event deposits through their different magnetic susceptibility, bulk density, and natural gamma radiation characteristics. Visual logging was also conducted on high-resolution core images to discern event layers via their different colors, textures, and structures from background deposits such as hemipelagic mud and laminations of calcareous ooze.

3.4. Primary chronology

Samples from holes U1499A and U1432C were analyzed for calcareous nannofossil and foraminiferal content, and biostratigraphic event identification (Li et al., 2015; Sun et al., 2018c). In addition, paleomagnetic studies have been conducted for the two holes by the IODP Scientific Parties. The Brunhes/Matuyama boundary (0.77 Ma) in holes U1499A (Sun et al., 2018c; Zhang et al., 2019) and U1432C (Li et al., 2015) is located at 116.3 m and 105.6 m, respectively. To conduct a detailed comparative study with Hole U1432C, we investigated the upper 120 m of Hole U1499A. In total, four microfossil ages and one paleomagnetic age are used to reconstruct the primary age-depth model of Hole U1499A (Fig. 3a; Table S3). In addition, five microfossil ages and one paleomagnetic age are used to reconstruct the primary age-depth model of Hole U1432C (Fig. 3b; Table S3). The microfossils of the holes were checked every ~6–10 m. Age uncertainties due to limited sample resolution are also considered (Fig. 3; Table S3).

4. Results

4.1. Basic types of event deposits and sediment facies

We identified pelagic mud, silty turbidites, sandy turbidites, mega-turbidites (meter-scale thickness), volcanic ash layers, three types of large-scale mass transport deposits (Fig. 4), and coring disturbances from the IODP core sections.

4.1.1. Pelagic mud, turbidite, volcanic ash, and turbidite-pelagic mud package

The units of pelagic mud are composed of clay and very fine silts without graded bedding. They commonly show massive and homogeneous textures, and small variations in magnetic susceptibility and bulk density (Fig. 4a, c). Occasionally, bioturbations can be found in these sediments. By contrast, turbidites are characterized by upward-fining grain size sequences and decreasing magnetic susceptibility, and bulk density from the base of the deposit to its top (Fig. 4a, c). Both silty and sandy turbidites are identified. The silty turbidites are composed of graded silts at their base with mud caps. The sandy turbidites are made up of graded coarse to fine sands at their base and finning to mud caps. The silty turbidities have weak erosion bases compared to the sandy turbidites which have sharp erosional contacts. For these turbidites, the ratio between the thickness of graded bedding (silty or sandy base) and

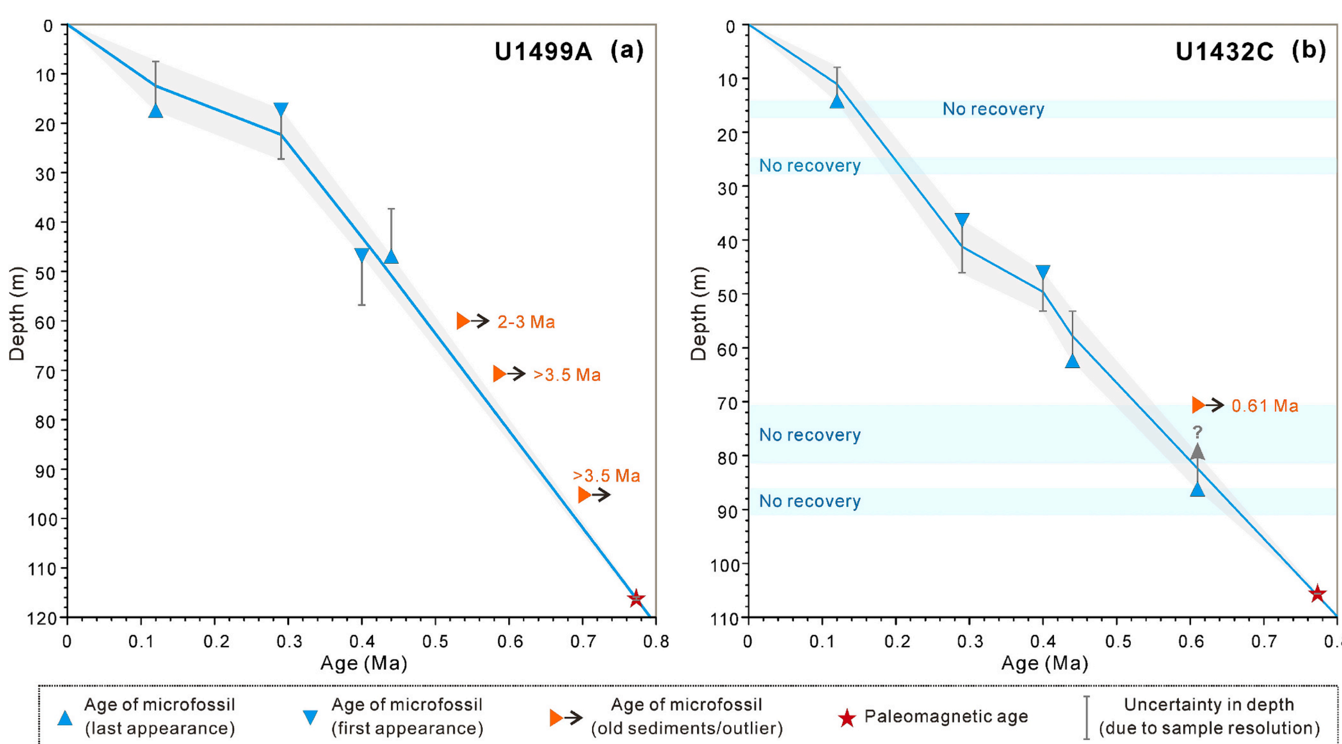

Fig. 3. Primary chronology of holes U1499A and U1432C. (a) Primary age-depth model of Hole U1499A; the paleomagnetic and microfossil ages from Zhang et al. (2019) and Sun et al. (2018a, 2018b, 2018c), respectively. (b) Primary age-depth model of Hole U1432C; the ages from Li et al. (2015) (Table S3).

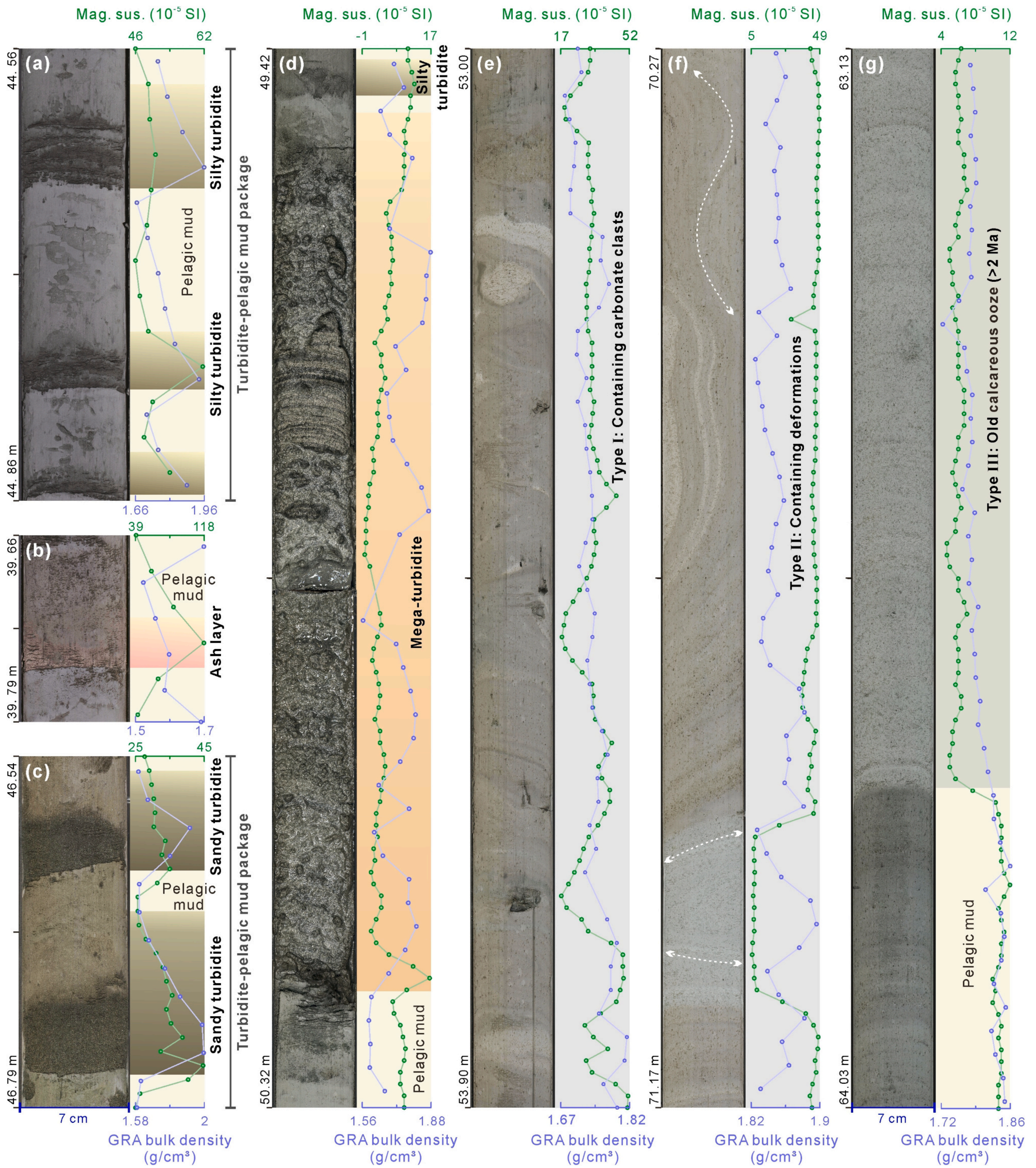

Fig. 4. Features of basic sediment facies and event deposits in holes U1499A and U1432C. (a) Pelagic mud and silty turbidites. (b) Pelagic mud and volcanic ash layer. (c) Pelagic mud and sandy turbidites. (d) Megaturbidite. (e-g) Type I-III large-scale mass transport deposits. Mag. Sus.: Magnetic susceptibility. GRA: Gamma ray attenuation. (a-b): from Hole U1432C; (c-g): from Hole U1499A.

mud tail is usually around 1.

We define meter-scale coarse sandy turbidite as megaturbidites. Megaturbidites are identified at 49.5 m (0.75 m thick) and 51.4 m (2.86 m thick) in holes U1499A and U1432C, respectively. These layers have a ratio of >7 in terms of the thickness of the graded sandy bases and their mud tops. Sharp erosional bases are observed at the base of these megaturbidites. In addition, parallel laminations are preserved in the megaturbidite from Hole U1499A (Fig. 4d). The megaturbidites show greater variability in physical characteristics than the other observed thinner turbidites (Fig. 4d). They show very low levels of magnetic susceptibility and exhibit decreasing magnetic susceptibility in their lower sections but an increasing trend in the upper part. Their bulk density shows frequent and large amplitude variations.

Volcanic ash layers show extremely high levels of magnetic susceptibility ($> 100 \times 10^{-5}$ SI) (Fig. 4b). Together, pelagic mud and turbidite deposits are commonly found to comprise turbidite-pelagic mud packages but show large variability in terms of the physical features exhibited by different couplets (Fig. 4a, c-d).

4.1.2. Three basic types of large-scale mass transport deposits

The Type I large-scale mass transport deposit units are characterized by soft carbonate clasts and chaotic structures (carbonates mixed with mud) (Fig. 4e). These units have a much higher bulk density than observed pelagic mud, but lower bulk density than measured turbidites. They also exhibit large variations in magnetic susceptibility. The Type II large-scale mass transport deposit units are characterized by folded thin beds of calcareous ooze (Fig. 4f). These units generally show much higher bulk density than the Type I large-scale mass transport deposits. The Type III large-scale mass transport deposit units are composed of older aged gray-colored carbonates (Fig. 4g). They contain microfossils with ages spanning from 2 Ma to >3.5 Ma, much older than the paleomagnetic age (0.77 Ma) of pelagic mud at the core depth of 116.3 m (Fig. 4g). This unit type shows very low magnetic susceptibility and small variations in physical features.

4.1.3. Coring disturbances

The upper 162 m of Hole U1499A and the entire Hole U1432C are cored using advanced piston corers. Thus, coring disturbances are expected to be preserved in the recovered two soft sedimentary sequences (Jutzeler et al., 2014). We observe three basic types of coring disturbances (Fig. 5). Type 1 disturbances are characterized by deformed laminations or thin beds that are entirely confined by the two sides of the core edge, and without layers, or beds confining the deformed structure at the top of it. This type of disturbance normally occurs on the top of a core section. Type 2 disturbances are characterized by symmetric deformation structures that are entirely confined by coring tubes with structure edges extending down core. Type 3 disturbances are characterized as cracks but without showing a regular fault line, and are therefore identifiable as different from syndepositional micro-faults.

4.2. Distribution of sediment facies and event deposits in the focused core intervals

In Hole U1499A, the lower (120.0–103.3 m) and upper (50.7–40.0 m) parts are characterized as turbidite-pelagic mud packages (Fig. 6).

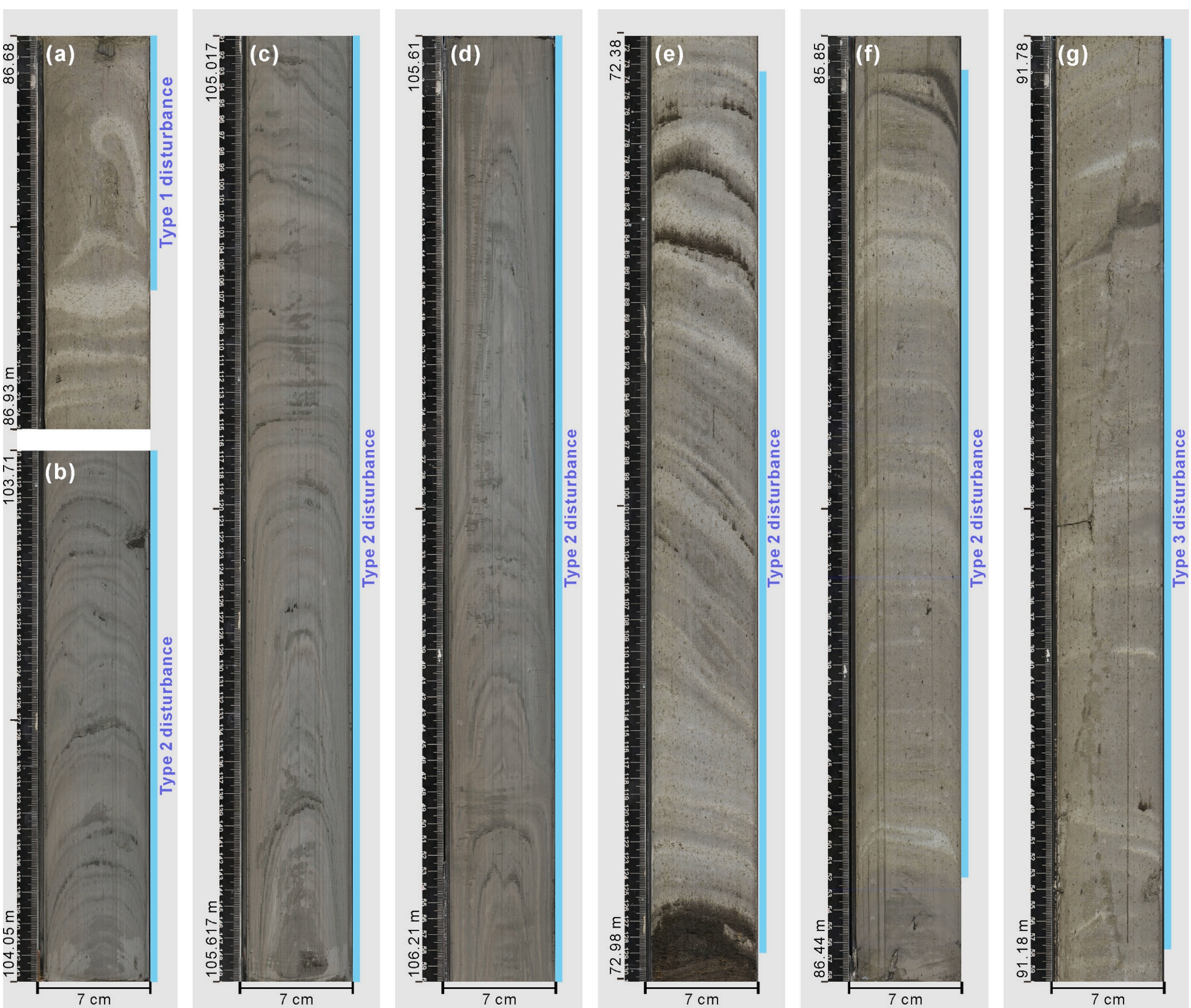

Fig. 5. Three basic types of coring disturbances in Hole U1499A. Type 1: disturbed thin beds entirely confined by the core edge. Type 2: moderate disturbed structures with edges extending toward the coring direction. Type 3: irregular crack.

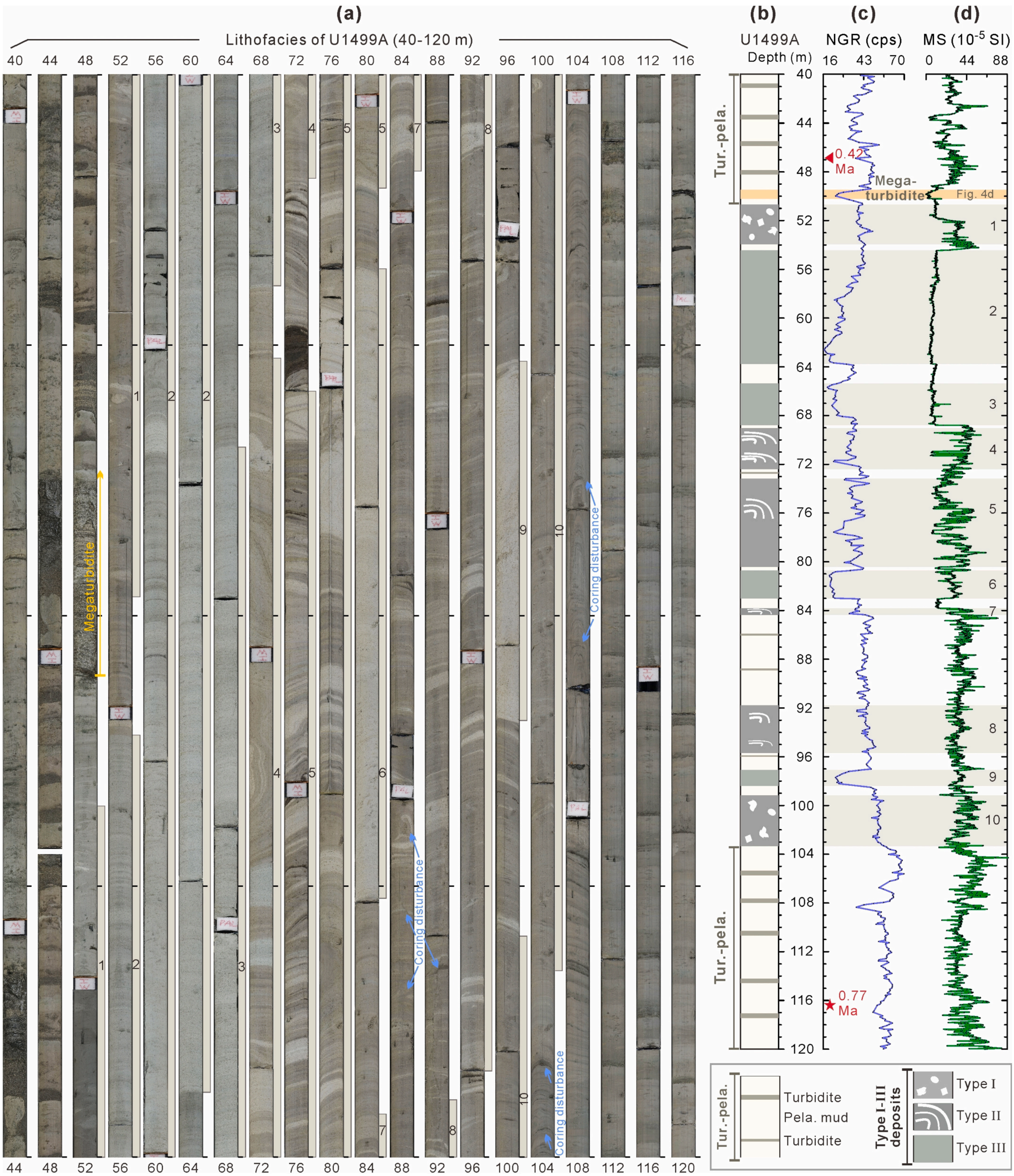

Fig. 6. Sedimentary facies and physical features of focused core interval (40–120 m) from Hole U1499A. (a) Core images showing sedimentary facies and event deposits. (b) Sediment facies and event deposits distribution. (c-d) Natural gamma radiation (NGR) and magnetic susceptibility (MS) characterize changes in physical features of the sedimentary sequence. Cps: counts per second. The numbers of 1 to 10 in (a) mark the deposit units indicated in (d). Tur.-pela.: turbidite-pelagic mud package. Core width: 7 cm.

The middle part (103.3–50.7 m) of the core mainly comprises two units of Type I mass transport deposits, four units of Type II mass transport deposits, and four units of Type III mass transport deposits. The 10 units of Type I-III mass transport deposits account for ~74% of the total thickness of the core interval 103.3–50.7 m.

Similarly, in Hole U1432C, the lower (110.0–81.5 m) and upper (54.5–39.0 m) parts are also expressed as turbidite-pelagic mud packages (Fig. 7). The middle part (81.5–54.5 m) mainly comprises three units of Type I mass transport deposits, two units of Type II mass transport deposits, and one interval without recovery (81.5–70.6 m). The five units of Type I-II mass transport deposits account for ~55% of the total recovered thickness of the core interval 81.5–54.5 m.

4.3. Event-free chronology

Type I-III mass transport deposits and megaturbidites are instantaneous deposits that may represent days to seconds in time duration. They account for ~50% and ~ 30% of the total thickness of recovered sediments in holes U1499A (upper 120 m) and U1432C, respectively. We refine the two primary age-depth models based on paleomagnetic and microfossil ages of the two holes by applying the idea of event-free chronology, i.e. instantaneous deposits are removed (Fig. 8a, b). The uncertainties resulting from microfossil sample resolution are also estimated by using the sediment accumulation rate of pelagic mud (Tables S4 and S5).

4.4. Ages of Type I-III mass transport deposits and megaturbidites

Based on our refined event-free age-depth model of the two drill holes (Fig. 8), we calculate the age of slumping units. This is achieved by assuming constant accumulation rates of hemipelagic mud between dated horizons. The accumulation rates of hemipelagic mud are derived

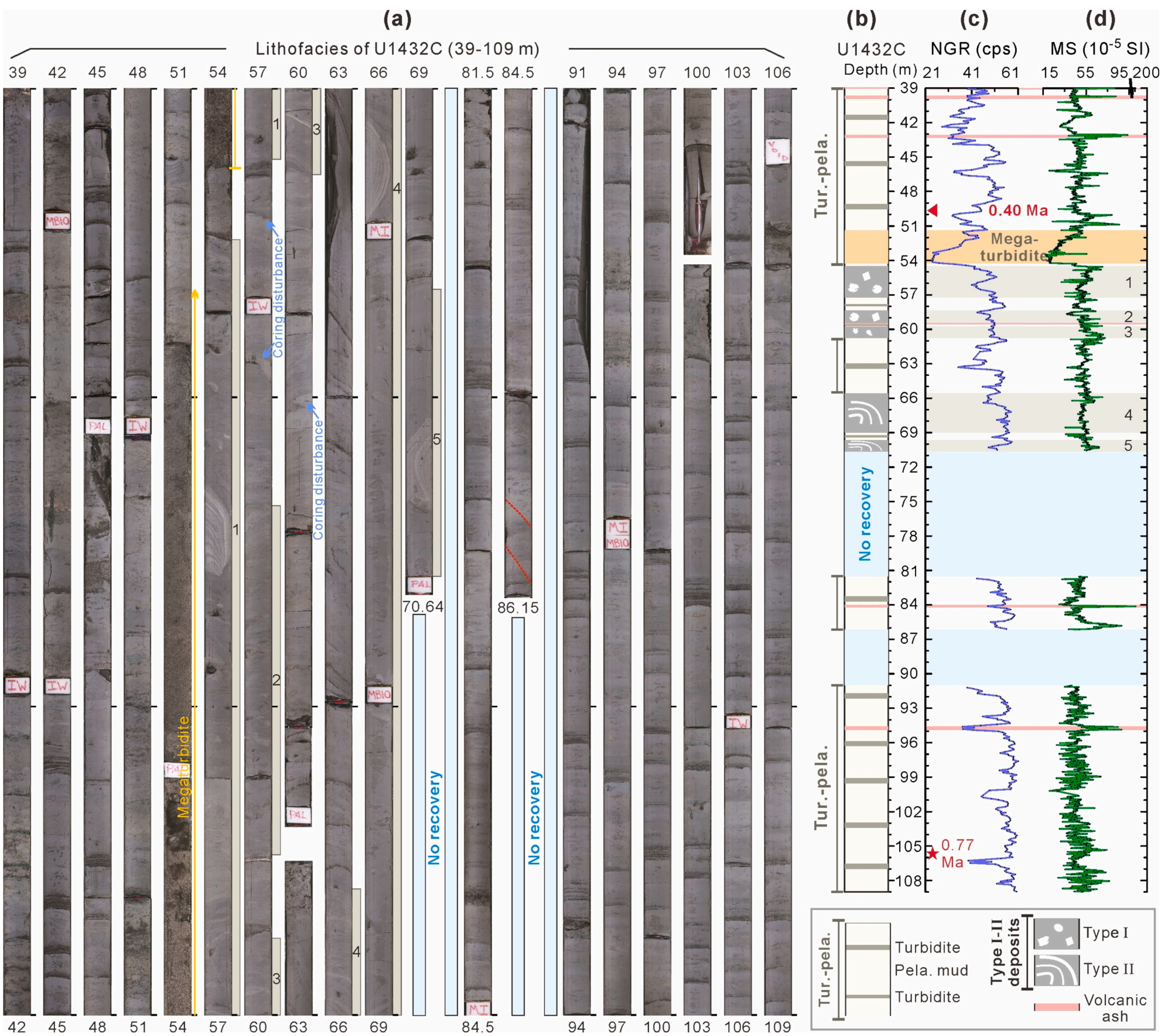

Fig. 7. Sedimentary facies and physical features of focused core interval (39–109 m) from Hole U1432C. (a) Core images showing sedimentary facies and event deposits. (b) Sediment facies and event deposits distribution. (c-d) Natural gamma radiation (NGR) and magnetic susceptibility (MS) characterize changes in physical features of the sedimentary sequence. Cps: counts per second. The numbers of 1 to 5 in (a) mark the deposit units indicated in (d). Tur.-pela.: turbidite-pelagic mud package. Core width: 7 cm.

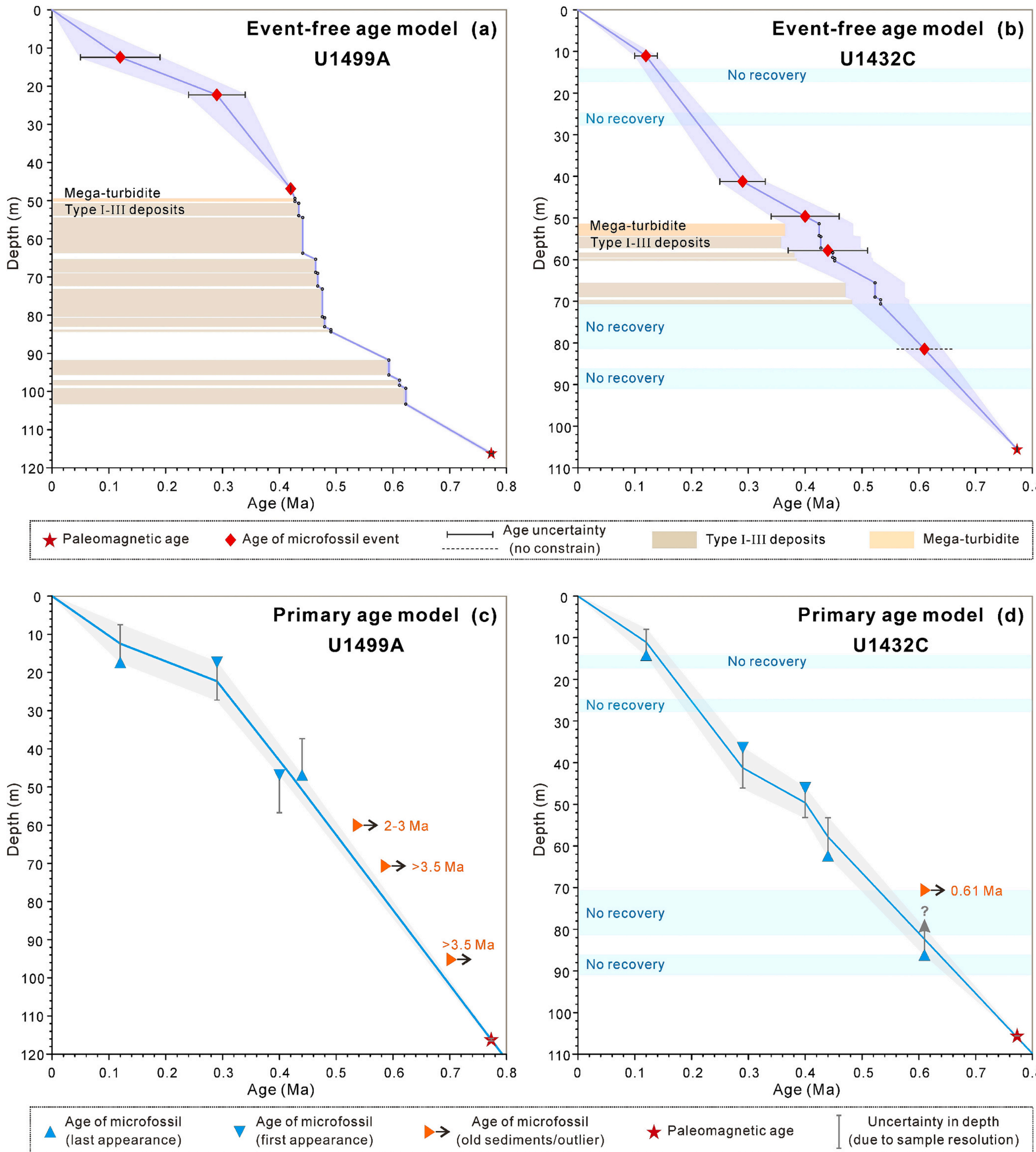

Fig. 8. Event-free chronology compared to primary chronology. (a) Event-free age model of Hole U1499A. (b) Event-free age model of Hole U1432C. (c) Primary age-depth model of Hole U1499A (same as Fig. 3a). (d) Primary age-depth model of Hole U1432C (same as Fig. 3b).

after deducting all event deposits, such as turbidites and slumping units. In Hole U1499A, the 10 layers of Type I-III mass transport deposits are deposited at 0.43 Ma, 0.44 Ma, 0.46 Ma, 0.47 Ma, 0.48 Ma, 0.48 Ma, 0.49 Ma, 0.60 Ma, 0.61 Ma, and 0.62 Ma, respectively (Fig. 8a; Table S6). In addition, the five layers of Type I-II mass transport deposits in Hole U1432C are emplaced at 0.43 Ma, 0.45 Ma, 0.45 Ma, 0.52 Ma, and 0.53 Ma, respectively (Fig. 8b; Table S6). The megaturbidites in holes U1499A and U1432C are both deposited at 0.43 Ma.

5. Discussion

Here we firstly discuss the sedimentary processes that formed the Type I-III mass transport deposits based on their distinct sedimentary textures. Secondly, we test our hypothesis that whether the thick chaotic seismic reflection is indeed a consequence of a giant slump event or a complex of multiple smaller events. Thirdly, we explore the recurrence behavior of the recovered slumping events. Finally, we discuss wider implications of our results for regional geohazards and their chronology.

5.1. Linking Type I-III mass transport deposits to slumping processes

The rounded shape of soft carbonate clasts in Type I mass transport deposits indicates these events likely underwent plastic debris flow processes and emplacement. In addition, the chaotic structures of Type I mass transport deposits imply that these sediments have experienced long-distance transportation and deformation (Lu et al., 2017). As a result, we identify these deposits as those typical of slumping processes, similar to those that have been previously reported from other continental subaqueous environments, such as the Dead Sea (Lu et al., 2017), the paleo-Qaidam Lake, NE Tibet (Lu et al., 2021), the New Jersey Margin (McHugh et al., 2002), the Nankai Trough (Strasser et al., 2011), and the Southern Alaskan Margin (Jaeger et al., 2014).

Soft folded laminations of calcareous ooze, like the characteristic structures in Type II deposits, can be induced either by an in situ deformation process (locally sourced) (Heifetz et al., 2005; Lu et al., 2020) or by a slumping process (ex situ process and remote sourced) (McHugh et al., 2002; Frey Martinez et al., 2005; Lu et al., 2017; Li et al., 2023). In situ deformation processes normally occur within well-laminated sediments that have stable density structures (in contrast to turbidite-pelagic mud deposits) and are initiated by earthquake-forced Kelvin-Helmholtz instabilities (Heifetz et al., 2005). Considering the passive margin setting of the northern South China Sea, a slumping process is more plausible for the deformation and is therefore favoured by the authors. The most likely source region for the slumping is the shallower upper-middle continental slope, which accumulates carbonate deposits as well as smaller volumes of sand (Fig. 1d).

Type III deposits are thick gray-colored carbonates. A previous study revealed that the carbonate compensation depth in the current study area is ~3800 m below sea level, which means the sedimentary $CaCO_3$ content would decrease to 0 at the water depth of the study site (Luo et al., 2018). When considering sea level and marine productivity

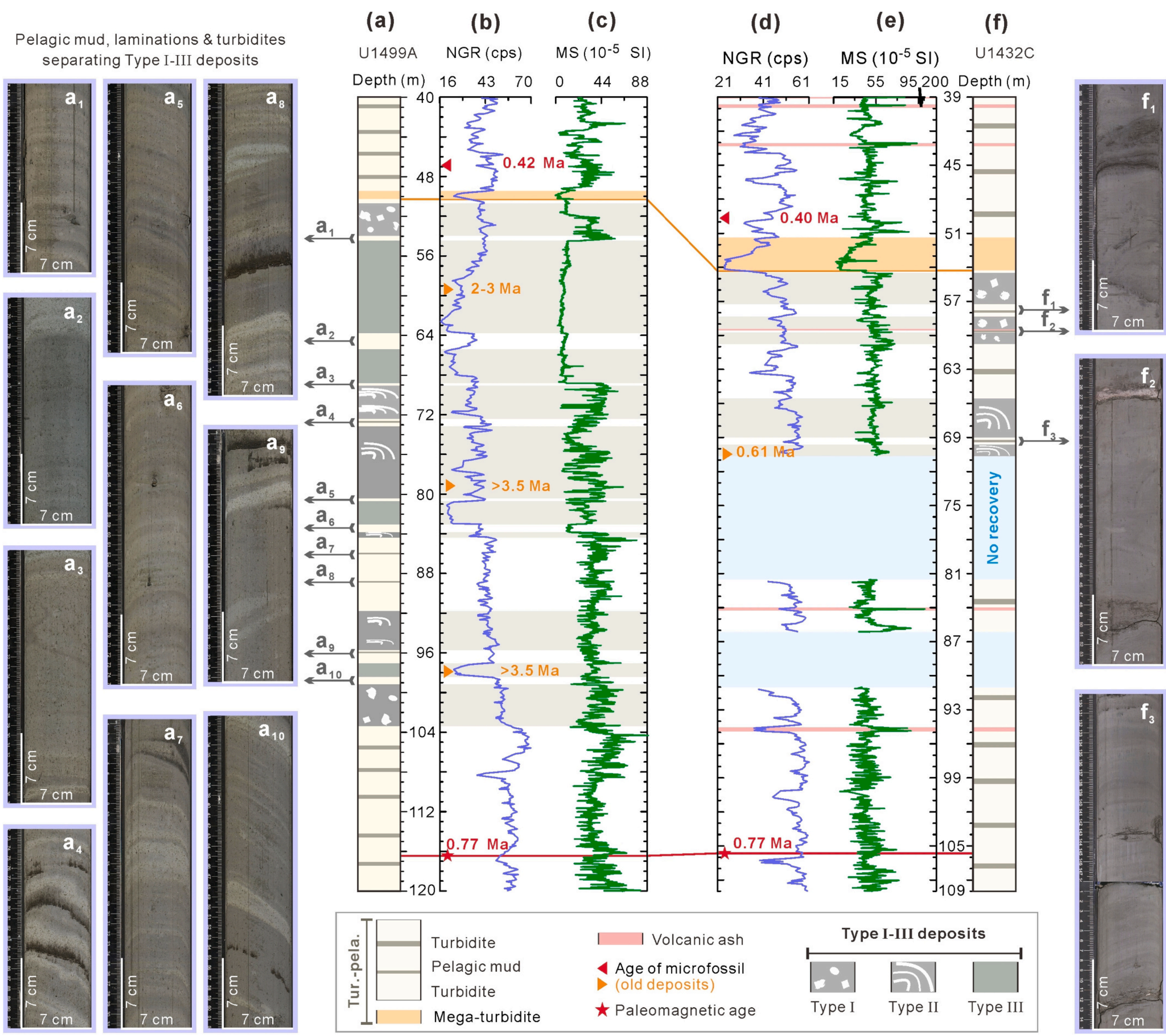

Fig. 9. Core images showing slumping units in holes U1499A and U1432C are separated by pelagic mud, laminations of calcareous ooze, and/or turbidites. (a_1-a_{10}) Core images showing pelagic mud/laminations (a_1-a_3, a_5, a_6, a_{10}), and turbidites (a_4, a_7-a_9) during the intervening of slump deposit units in Hole U1499A. (b-e) Change in physical features of the two focused sedimentary sequences. (f_1-f_3) Core images showing turbidites (f_1), volcanic ash layer (f_2), and pelagic mud/laminations (f_3) during the intervening of slump deposit units in Hole U1432C. Tur.-pela.: turbidite-pelagic mud package.

fluctuations during Quaternary glacial cycles, we estimate the $CaCO_3$ content of in situ sediments at U1499 (water depth: ~3770 m) and U1432 (water depth: ~3840 m) sites ranged between ~2%–1% and ~1%–0%, respectively (Luo et al., 2018). Therefore, the Type III deposits are not likely to have been accumulated in situ. Microfossils from Type III deposits are also older than 2 Ma (Sun et al., 2018c), which is much older than the ages of underlying pelagic mud sequences.

Several IODP and ODP holes from the nearby continental slope region (Fig. 1b) both contained Quaternary sediments characterized by greenish-gray clay-rich nannofossil ooze with high carbonate contents (Fig. 1d) (Wang et al., 2000; Sun et al., 2018c). A significant hiatus occurred during 12–2 Ma has been identified at Site U1504 from the lower slope (Fig. 1b) (Sun et al., 2018c). The age of the hiatus matches the age of Type III deposits at Site U1499. We therefore link the Type III deposits to continental slope failures and related slumping, and mass flow processes.

5.2. Testing hypothesis

Type I, Type II, and Type III mass transport deposits in Holes U1499A and U1432C are consequences of slope failures and slumping processes in the Pearl River Canyon, Baiyun Sag. In the two holes, the thick slumping units are separated by pelagic mud, laminations of calcareous ooze, and/or turbidites (Fig. 9a_1-a_{10}). Their preservation indicates these sediments have no direct relationship with the slumping processes that resulted in the thick slump deposits. These results suggest that the previously interpreted single ~50 m-thick slump unit in Hole U1499A is a complex of multiple moderate to large-scale slump units.

The microfossil age of 0.4 Ma and the paleomagnetic age of 0.77 Ma are first-order control points to correlate the strata in holes U1499A and U1432C (Fig. 9). The upper and lower parts of the two core intervals in question also show very similar trends in the variation of natural gamma radiation and magnetic susceptibility (Fig. 9), and suggesting good correlation with one another. Hole U1432C also shows multiple slumping units separated by pelagic mud, turbidites, and/or volcanic ash layers during 0.6–0.4 Ma. The distribution of sediment facies and event deposits in the two holes therefore supports our hypothesis that the ~50 m-thick chaotic seismic reflection represents a complex of multiple moderate slumping units and not a single mass failure event.

5.3. Clustered slumping behavior

We calculated descriptive statistics based on the recurrence intervals of these slumping events. The coefficient of variation (standard deviation divided by mean) of recurrence intervals is the most commonly used dimensionless parameter to describe the occurrence behavior of catastrophic events (Kagan and Jackson, 1991; Berryman et al., 2012; Moernaut, 2020). Normally, a record with a coefficient of variation ≥1.2

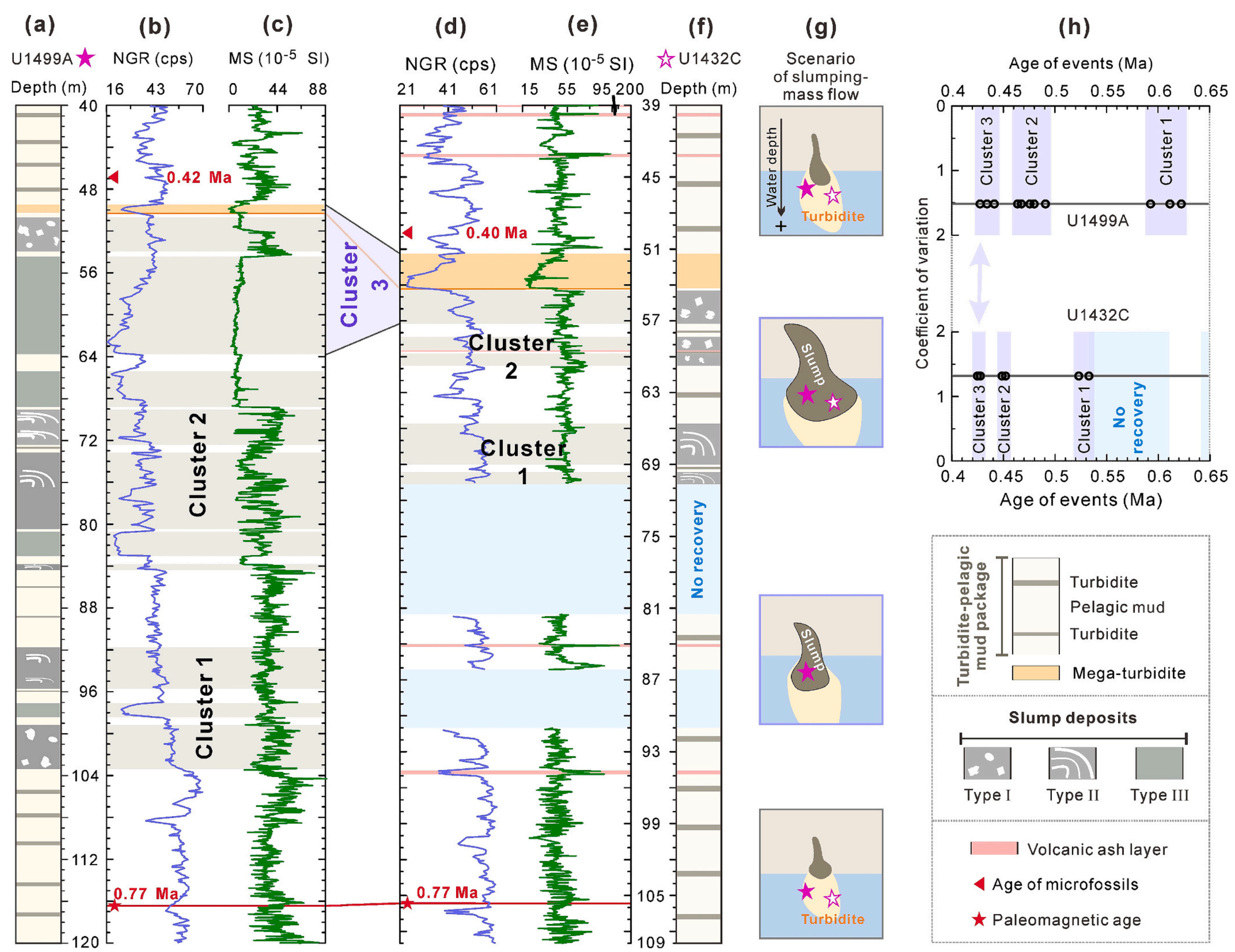

Fig. 10. Clustered slumping behavior was recorded by the sedimentary sequences of holes U1499A and U1432C. (a-f) Sedimentary records. (g) Schematic models showing correspondence sedimentary scenarios. (h) Clustered distribution of the events recorded in the two holes.

is defined as "clustered" behavior (Kagan and Jackson, 1991; Berryman et al., 2012; Moernaut, 2020). The coefficient of variation of identified events from Hole U1499A and Hole U1432C are ~1.5 and ~ 1.3, respectively (Fig. 10). This suggests that these events are clustered in time. These events can be grouped into three clusters within each hole (Fig. 10h).

Marine slope failure and slumping usually initiate turbidity currents in front of the main body of the slump (Sun et al., 2018a). These more dilute flows tend to have longer run-out distances and therefore transport sediment further. Site U1499 is closer to the toe of the Pearl River Canyon than Site U1432, and also 70 m shallower than Site U1432. Event cluster 3 can be correlated across both boreholes. However, the other event clusters are not recorded simultaneously in the two holes. This may either be due to the certain distance between the boreholes (~50 km) or different event magnitudes occurring, or different slump translation speeds, or contrasting sediment stack characteristics, i.e. levels of consolidation (Fig. 10g).

5.4. Wider implications

A comprehensive understanding of the links between sedimentary processes, deposits, and sediment facies is vital for event identification from subaqueous drill cores. In active subaqueous environments, such as the Dead Sea (Lu et al., 2022), Lake Van (Turkey) (Stockhecke et al., 2014), the Gulf of Corinth (De Gelder et al., 2022), and the Nankai Trough (Kremer et al., 2017), the thickness fraction of slump deposits, turbidites, and/or debrites can reach to 10–30% of total recovered sedimentary sequences. This fraction could be even >50% during some specific time intervals when marine slumping frequently occurs, e.g., the Dead Sea during the last glacial period (Lu et al., 2017). Indeed, where these events are common, identification and removal of such events are critical to the establishment of accurate age-depth models. This is crucial where these models underpin local hazard assessments.

In the northern South China Sea, previous studies have interpreted the ~50 m-thick strata as one thick slumping unit by using seismic reflection data (Hole U1499A; e.g., Sun et al., 2018c). Based on this interpretation, the ~50 m-thick sediments were entirely removed from age-depth modeling for Hole U1499A (Zhang et al., 2019). Our presented high-resolution sedimentological investigation on these sediments reveals that slumping deposits only make up ~75% of the ~50 m-thick core interval. Our event-free chronology of Hole U1499A yields an average event-free sediment accumulation rate of ~7 cm/kyr for the period of 0.8–0.4 Ma, similar to the average rate of ~6 cm/kyr for the period of 1.0–0.8 Ma. This implies that background sedimentation rates in the region have not greatly changed during 1.0–0.4 Ma.

In many regions where recorded histories of natural hazards are short, which is particularly true for many subaqueous environments, our understanding of geohazards and their long-term behavior relies on preserved deposits in the geological record (Kremer et al., 2012; Gauchery et al., 2021). In the South China Sea, multiple slumping events have been identified using seismic reflection and multibeam data (Sun et al., 2018b). Some of them have been modeled to understand their potential to generate damaging tsunamis. These studies have suggested that slumping events in the northern part of the South China Sea could be tsunamigenic and thus may represent a largely unrecognized geohazard for the coastlines of the South China Sea (Sun et al., 2022). Since event frequency and magnitude are two important parameters for geohazard assessment, the identification of more(fewer) events of smaller (larger) magnitude has the potential to alter local/regional risk assessments. The combined use of seismic reflection data and detailed sediment core investigations are therefore an important means to achieve more accurate geohazard assessments and inform potentially impacted communities.

In summary, the identification of event deposits is important for developing more reliable and accurate age-depth models. This is important, not only for further high-resolution paleoclimate studies but also for dating and reconstructing geohazard events and assessment of catastrophic risk. This study highlights the importance of combining these methods to accurately identify event deposits from marine sedimentary sequences. Our high-resolution sedimentological method to discern event deposits may also prove suitable for IODP, ICDP, and other scientific drill cores in both passive and active subaqueous environments.

6. Conclusions

We investigate event deposits in the IODP holes U1499A and U1432C which are 50 km apart from each other in the northern South China Sea deep basin, combining multiple methods. We identify three basic types of slumping deposits through sedimentary structure analysis and consideration of carbonate compensation depth variation and microfossil age distribution. The slumping deposits are linked to slope failures that occurred in the NE South China Sea continental slope. We find that (1) the previously interpreted single thick slumping unit is a complex of multiple moderate-sized slump deposits; (2) the slumping events are clustered between 0.6 and 0.4 Ma. We derive high-resolution event-free age-depth models for holes U1499A and U1432C and have the potential to gain a better understanding of regional catastrophic risk by proper identification of event deposits.

CRediT authorship contribution statement

Yin Lu: Conceptualization, analysis, validation, writing original draft, funding acquisition, project administration. **Ed L. Pope:** Validation, review & editing. **Qiliang Sun:** Validation, review & editing. **Michael Strasser:** Validation, review & editing.

Declaration of competing interest

The authors declare that they have no known competing financial interests or personal relationships that could have appeared to influence the work reported in this paper.

Acknowledgments

This research used data provided by the International Ocean Discovery Program (IODP). The work was supported by the Chinese National Natural Science Fund for Excellent Young Scientists Fund Program (Overseas) (to Y. Lu) and the Chinese Fundamental Research Funds for the Central Universities (#22120240219 to Y. Lu). We thank Zhifei Liu for supporting this research and participating in the IODP campaigns, and Yulong Zhao, Nan Wu, and Yakufu Niyazi for their helpful discussions and comments. The authors appreciate Wei Li and an anonymous reviewer for thorough and constructive reviews, and the editors Jimin Sun and Wenfeng Deng for handling the manuscript.

Appendix A. Supplementary data

Supplementary data to this article can be found online at https://doi.org/10.1016/j.gloplacha.2024.104623.

Data availability

Datasets are available in the Supplementary Material.

References

Berndt, C., Costa, S., Canals, M., Camerlenghi, A., de Mol, B., Saunders, M., 2012. Repeated slope failure linked to fluid migration: the Ana submarine landslide complex, Eivissa Channel, Western Mediterranean Sea. Earth Planet. Sci. Lett. 319-320, 65–74. https://doi.org/10.1016/j.epsl.2011.11.045.

Berryman, K.R., Cochran, U.A., Clark, K.J., Biasi, G.P., Langridge, R.M., Villamor, P., 2012. Major earthquakes occur regularly on an isolated plate boundary fault. Science 336, 1690–1693.

Bull, S., Cartwright, J., Huuse, M., 2009. A review of kinematic indicators from mass-transport complexes using 3D seismic data. Mar. Pet. Geol. 26, 1132–1151. https://doi.org/10.1016/j.marpetgeo.2008.09.011.

Coianiz, L., Ben-Avraham, Z., Stein, M., Lazar, M., 2019. Spatial and temporal reconstruction of the late Quaternary Dead Sea sedimentary facies from geophysical properties. J. Appl. Geophys. 160, 15–27. https://doi.org/10.1016/j.jappgeo.2018.11.002.

Cukur, D., Krastel, S., Schmincke, H.-U., Sumita, M., Çağatay, M.N., Meydan, A.F., Damcı, E., Stockhecke, M., 2014. Seismic stratigraphy of Lake Van, eastern Turkey. Quat. Sci. Rev. https://doi.org/10.1016/j.quascirev.2014.07.016.

De Gelder, G., Doan, M.L., Beck, C., Carlut, J., Seibert, C., Feuillet, N., Carter, G.D.O., Pechlivanidou, S., Gawthorpe, R.L., McArthur, A., 2022. Multi-scale and multi-parametric analysis of Late Quaternary event deposits within the active Corinth Rift (Greece). Sedimentology 69, 1573–1598. https://doi.org/10.1111/sed.12964.

Díaz-Curiel, J., Miguel, M.J., Biosca, B., Arévalo-Lomas, L., 2021. Gamma ray log to estimate clay content in the layers of water boreholes. J. Appl. Geophys. 195, 104481. https://doi.org/10.1016/j.jappgeo.2021.104481.

Ding, W., Li, J., Li, J., Fang, Y., Tang, Y., 2013. Morphotectonics and evolutionary controls on the Pearl River Canyon system, South China Sea. Mar. Geophys. Res. 34, 221–238. https://doi.org/10.1007/s11001-013-9173-9.

Ding, W., Sun, Z., Dadd, K., Fang, Y., Li, J., 2018. Structures within the oceanic crust of the central South China Sea basin and their implications for oceanic accretionary processes. Earth Planet. Sci. Lett. 488, 115–125. https://doi.org/10.1016/j.epsl.2018.02.011.

Ding, W., Sun, Z., Mohn, G., Nirrengarten, M., Tugend, J., Manatschal, G., Li, J., 2020. Lateral evolution of the rift-to-drift transition in the South China Sea: evidence from multi-channel seismic data and IODP Expeditions 367&368 drilling results. Earth Planet. Sci. Lett. 531, 115932. https://doi.org/10.1016/j.epsl.2019.115932.

Ford, J., Urgeles, R., Camerlenghi, A., Gràcia, E., 2021. Seismic diffraction imaging to characterize mass-transport complexes: examples from the Gulf of Cadiz, South West Iberian margin. J. Geophys. Res. Solid Earth 126, e2020JB021474. https://doi.org/10.1029/2020jb021474.

Frey Martinez, J., Cartwright, J., Hall, B., 2005. 3D seismic interpretation of slump complexes: examples from the continental margin of Israel. Basin Res. 17, 83–108. https://doi.org/10.1111/j.1365-2117.2005.00255.x.

Gauchery, T., Rovere, M., Pellegrini, C., Cattaneo, A., Campiani, E., Trincardi, F., 2021. Factors controlling margin instability during the Plio-Quaternary in the Gela Basin (Strait of Sicily, Mediterranean Sea). Mar. Pet. Geol. 123, 104767. https://doi.org/10.1016/j.marpetgeo.2020.104767.

Harris, P.T., Whiteway, T., 2011. Global distribution of large submarine canyons: geomorphic differences between active and passive continental margins. Mar. Geol. 285, 69–86. https://doi.org/10.1016/j.margeo.2011.05.008.

He, Y., Zhong, G., Wang, L., Kuang, Z., 2014. Characteristics and occurrence of submarine canyon-associated landslides in the middle of the northern continental slope, South China Sea. Mar. Pet. Geol. 57, 546–560. https://doi.org/10.1016/j.marpetgeo.2014.07.003.

Heider, F., Ko, U., Bitschene, P., 1993. Volcanic ash particles as carriers of remanent magnetization in deep-sea sediments from the Kerguelen Plateau. Earth Planet. Sci. Lett. 118, 121–134.

Heifetz, E., Agnon, A., Marco, S., 2005. Soft sediment deformation by Kelvin Helmholtz Instability: a case from Dead Sea earthquakes. Earth Planet. Sci. Lett. 236, 497–504. https://doi.org/10.1016/j.epsl.2005.04.019.

Jaeger, J.M., Gulick, S.P.S., LeVay, L.J., Asahi, H., Bahlburg, H., Belanger, C.L., 2014. Proceedings of the Integrated Ocean Drilling Program, Volume 341, Site U1418. https://doi.org/10.2204/iodp.proc.341.104.2014.

Jutzeler, M., White, J.D.L., Talling, P.J., McCanta, M., Morgan, S., Le Friant, A., Ishizuka, O., 2014. Coring disturbances in IODP piston cores with implications for offshore record of volcanic events and the Missoula megafloods. Geochem. Geophys. Geosyst. 15, 3572–3590. https://doi.org/10.1002/2014gc005447.

Kagan, Y.Y., Jackson, D.D., 1991. Long-term earthquake clustering. Geophys. J. Int. 104, 117–133.

Karstens, J., Berndt, C., Urlaub, M., Watt, S.F.L., Micallef, A., Ray, M., Klaucke, I., Muff, S., Klaeschen, D., Kühn, M., et al., 2019. From gradual spreading to catastrophic collapse – Reconstruction of the 1888 Ritter Island volcanic sector collapse from high-resolution 3D seismic data. Earth Planet. Sci. Lett. 517, 1–13. https://doi.org/10.1016/j.epsl.2019.04.009.

Kluesner, J., Brothers, D., Hart, P., Miller, N., Hatcher, G., 2018. Practical approaches to maximizing the resolution of sparker seismic reflection data. Mar. Geophys. Res. 40, 279–301. https://doi.org/10.1007/s11001-018-9367-2.

Kremer, K., Simpson, G., Girardclos, S., 2012. Giant Lake Geneva tsunami in AD 563. Nat. Geosci. 5, 756–757. https://doi.org/10.1038/ngeo1618.

Kremer, K., Usman, M.O., Satoguchi, Y., Nagahashi, Y., Vadakkepuliyambatta, S., Panieri, G., Strasser, M., 2017. Possible climate preconditioning on submarine landslides along a convergent margin, Nankai Trough (NE Pacific). Prog. Earth Planet Sci. 4. https://doi.org/10.1186/s40645-017-0134-9.

Larsen, H.C., Mohn, G., Nirrengarten, M., Sun, Z., Stock, J., Jian, Z., Klaus, A., Alvarez-Zarikian, C.A., Boaga, J., Bowden, S.A., et al., 2018. Rapid transition from continental breakup to igneous oceanic crust in the South China Sea. Nat. Geosci. 11, 782–789. https://doi.org/10.1038/s41561-018-0198-1.

Le Pourhiet, L., Chamot-Rooke, N., Delescluse, M., May, D.A., Watremez, L., Pubellier, M., 2018. Continental break-up of the South China Sea stalled by far-field compression. Nat. Geosci. 11, 605–609. https://doi.org/10.1038/s41561-018-0178-5.

Li, W., Wu, S., Völker, D., Zhao, F., Mi, L., Kopf, A., 2014. Morphology, seismic characterization and sediment dynamics of the Baiyun Slide Complex on the northern South China Sea margin. J. Geol. Soc. Lond. 171, 865–877. https://doi.org/10.1144/jgs2014-034.

Li, C.-F., Lin, J., Kulhanek, D., Williams, T., Bao, R., Briais, A., Brown, E., Chen, Y., Clift, P., Colwell, F., 2015. Expedition 349 summary. In: Proceedings of the International Ocean Discovery Program, 349. https://doi.org/10.14379/iodp.proc.349.101.2015.

Li, W., Alves, T.M., Rebesco, M., Sun, J., Li, J., Li, S., Wu, S., 2020. The Baiyun Slide Complex, South China Sea: a modern example of slope instability controlling submarine-channel incision on continental slopes. Mar. Pet. Geol. 114, 104231. https://doi.org/10.1016/j.marpetgeo.2020.104231.

Li, W., Li, Y., Omosanya, K.O.L., Alves, T.M., Jing, S., Wang, X., Wu, N., Zhan, W., 2023. Quantitative and geomorphologic parameterization of megaclasts within mass-transport complexes, offshore Taranaki Basin, New Zealand. GSA Bull. 135, 1828–1843. https://doi.org/10.1130/b36446.1.

Liu, Z., Zhao, Y., Colin, C., Stattegger, K., Wiesner, M.G., Huh, C.-A., Zhang, Y., Li, X., Sompongchaiyakul, P., You, C.-F., et al., 2016. Source-to-sink transport processes of fluvial sediments in the South China Sea. Earth Sci. Rev. 153, 238–273. https://doi.org/10.1016/j.earscirev.2015.08.005.

Liu, J., Chang, Q., Zhang, J., Chai, H., He, F., Yang, Y., Xia, S., 2023. The determination of sedimentary environment and associated energy in deep-buried marine carbonates: insights from natural gamma ray spectrometry log. Front. Earth Sci. 18, 204–218. https://doi.org/10.1007/s11707-022-1053-7.

Lu, Y., Waldmann, N., Ian Alsop, G., Marco, S., 2017. Interpreting soft sediment deformation and mass transport deposits as seismites in the Dead Sea depocenter. J. Geophys. Res. Solid Earth 122, 8305–8325. https://doi.org/10.1002/2017JB014342.

Lu, Y., Wetzler, N., Waldmann, N., Agnon, A., Biasi, G., Marco, S., 2020. A 220,000-year-long continuous large earthquake record on a slow-slipping plate boundary. Sci. Adv. 6, eaba4170. https://doi.org/10.1126/sciadv.aba4170.

Lu, Y., Marco, S., Wetzler, N., Fang, X., Alsop, I., Hubert-Ferrari, A., 2021. A paleoseismic record spanning 2-Myr reveals episodic late Pliocene deformation in the western Qaidam Basin, NE Tibet. Geophys. Res. Lett. 48, e2020GL090530. https://doi.org/10.1029/2020GL090530.

Lu, Y., Pope, E.L., Moernaut, J., Bookman, R., Waldmann, N., Agnon, A., Marco, S., Strasser, M., 2022. Stratigraphic record reveals contrasting roles of overflows and underflows over glacial cycles in a hypersaline lake (Dead Sea). Earth Planet. Sci. Lett. 594, 117723. https://doi.org/10.1016/j.epsl.2022.117723.

Luo, Y., Kienast, M., Boudreau, B.P., 2018. Invariance of the carbonate chemistry of the South China Sea from the glacial period to the Holocene and its implications to the Pacific Ocean carbonate system. Earth Planet. Sci. Lett. 492, 112–120. https://doi.org/10.1016/j.epsl.2018.04.005.

McHugh, C.M., Damuth, J.E., Mountain, G.S., 2002. Cenozoic mass-transport facies and their correlation with relative sea-level change, New Jersey continental margin. Mar. Geol. 184, 295–334.

Miller, K.G., Browning, J.V., Schmelz, W.J., Kopp, R.E., Mountain, G.S., Wright, J.D., 2020. Cenozoic sea-level and cryospheric evolution from deep-sea geochemical and continental margin records. Sci. Adv. 6, eaaz1346. https://doi.org/10.1126/sciadv.aaz1346.

Milliman, J.D., Farnsworth, K.L., 2011. River Discharge to the Coastal Ocean: A Global Synthesis. Cambridge University Press, Cambridge, England.

Moernaut, J., 2020. Time-dependent recurrence of strong earthquake shaking near plate boundaries: a lake sediment perspective. Earth Sci. Rev. 210, 103344. https://doi.org/10.1016/j.earscirev.2020.103344.

Olson, H., Damuth, J., 2010. Character, distribution and timing of latest quaternary mass-transport deposits in Texas-Louisiana intraslope basins based on high-resolution (3.5 kHz) seismic facies and piston cores. In: Mosher, D.C., Shipp, R.C., Moscardelli, L., Chaytor, J.D., Baxter, C.D.P., Lee, H.J., Urgeles, R. (Eds.), Submarine Mass Movements and their Consequences. Springer, Dordrecht, pp. 607–617.

Posamentier, H.W., Kolla, V., 2003. Seismic geomorphology and stratigraphy of depositional elements in deep-water settings. J. Sediment. Res. 73, 367–388.

Roksandić, M., 1978. Seismic facies analysis concepts. Geophys. Prospect. 26, 383–398.

Schwarz, B., Krawczyk, C.M., 2020. Coherent diffraction imaging for enhanced fault and fracture network characterization. Solid Earth 11, 1891–1907. https://doi.org/10.5194/se-11-1891-2020.

Stockhecke, M., Sturm, M., Brunner, I., Schmincke, H.U., Sumita, M., Kipfer, R., Cukur, D., Kwiecien, O., Anselmetti, F.S., Ariztegui, D., 2014. Sedimentary evolution and environmental history of Lake Van (Turkey) over the past 600,000 years. Sedimentology 61, 1830–1861. https://doi.org/10.1111/sed.12118.

Strasser, M., Moore, G.F., Kimura, G., Kopf, A.J., Underwood, M.B., Guo, J., Screaton, E. J., 2011. Slumping and mass transport deposition in the Nankai fore arc: evidence from IODP drilling and 3-D reflection seismic data. Geochem. Geophys. Geosyst. 12, Q0AD13. https://doi.org/10.1029/2010gc003431.

Sun, Y.B., Wu, S.G., Wang, Z.J., Li, Q.P., Wang, X.J., Dong, D.D., Liu, F., 2008. The geometry and deformation characteristics of Baiyun Submarine Landslide. Mar. Geol. Quat. Geol. (in Chinese with English abstract) 28, 70–77. https://doi.org/10.3724/sp.j.1140.2008.06069.

Sun, Q., Alves, T., Xie, X., He, J., Li, W., Ni, X., 2017a. Free gas accumulations in basal shear zones of mass-transport deposits (Pearl River Mouth Basin, South China Sea): an important geohazard on continental slope basins. Mar. Pet. Geol. 81, 17–32. https://doi.org/10.1016/j.marpetgeo.2016.12.029.

Sun, Q., Xie, X., Piper, D.J.W., Wu, J., Wu, S., 2017b. Three dimensional seismic anatomy of multi-stage mass transport deposits in the Pearl River Mouth Basin, northern South China Sea: their ages and kinematics. Mar. Geol. 393, 93–108. https://doi.org/10.1016/j.margeo.2017.05.005.

Sun, Q., Alves, T.M., Lu, X., Chen, C., Xie, X., 2018a. True volumes of slope failure estimated from a quaternary mass-transport deposit in the Northern South China Sea. Geophys. Res. Lett. 45, 2642–2651. https://doi.org/10.1002/2017gl076484.

Sun, Q., Cartwright, J., Xie, X., Lu, X., Yuan, S., Chen, C., 2018b. Reconstruction of repeated Quaternary slope failures in the northern South China Sea. Mar. Geol. 401, 17–35. https://doi.org/10.1016/j.margeo.2018.04.009.

Sun, Z., Jian, Z., Stock, J., Larsen, H., Klaus, A., Zarikian, C.A., 2018c. Expedition 367/368 summary. In: Proceedings of the International Ocean Discovery Program, 367/368. https://doi.org/10.14379/iodp.proc.367368.101.2018.

Sun, Z., Ding, W., Zhao, X., Qiu, N., Lin, J., Li, C.F., 2019. The latest spreading periods of the South China Sea: new constraints from macrostructure analysis of IODP expedition 349 cores and geophysical data. J. Geophys. Res. Solid Earth 124, 9980–9998. https://doi.org/10.1029/2019jb017584.

Sun, Q., Wang, Q., Shi, F., Alves, T., Gao, S., Xie, X., Wu, S., Li, J., 2022. Runup of landslide-generated tsunamis controlled by paleogeography and sea-level change. Commun. Earth Environ. 3. https://doi.org/10.1038/s43247-022-00572-w.

Vigliotti, L., Bilardello, D., Winkler, A., Del Carlo, P., 2022. Rock magnetic fingerprint of Mt Etna volcanic ash. Geophys. J. Int. 231, 749–769. https://doi.org/10.1093/gji/ggac213.

Wang, P., Prell, W., Blum, P., Arnold, E., Bühring, C., Chen, M., Clemens, S., Clift, P., Colin, C., Farrell, J., 2000. Exploring the Asian monsoon through drilling in the South China Sea. JOIDES J. 25, 8–13.

Wang, L., Wu, S.-G., Li, Q.-P., Wang, D.-W., Fu, S.-Y., 2014. Architecture and development of a multi-stage Baiyun submarine slide complex in the Pearl River Canyon, northern South China Sea. Geo-Mar. Lett. 34, 327–343. https://doi.org/10.1007/s00367-014-0372-4.

Wang, X., Wang, Y., He, M., Chen, W., Zhuo, H., Gao, S., Wang, M., Zhou, J., 2017. Genesis and evolution of the mass transport deposits in the middle segment of the Pearl River canyon, South China Sea: insights from 3D seismic data. Mar. Pet. Geol. 88, 555–574. https://doi.org/10.1016/j.marpetgeo.2017.08.036.

Xu, G., Haq, B.U., 2022. Seismic facies analysis: past, present and future. Earth Sci. Rev. 224, 103876. https://doi.org/10.1016/j.earscirev.2021.103876.

Zhang, Y., Yi, L., Ogg, J.G., 2019. Pliocene-Pleistocene magneto-cyclostratigraphy of IODP Site U1499 and implications for climate-driven sedimentation in the northern South China Sea. Palaeogeogr. Palaeoclimatol. Palaeoecol. 527, 118–132. https://doi.org/10.1016/j.palaeo.2019.04.029.

Zhu, M., Graham, S., Pang, X., McHargue, T., 2010. Characteristics of migrating submarine canyons from the middle Miocene to present: implications for paleoceanographic circulation, northern South China Sea. Mar. Pet. Geol. 27, 307–319. https://doi.org/10.1016/j.marpetgeo.2009.05.005.